



HAL
open science

Thermal heterogeneity within aqueous materials quantified by ^1H NMR spectroscopy: Multiparametric validation *in silico* and *in vitro*

Norbert W Lutz, Monique Bernard

► **To cite this version:**

Norbert W Lutz, Monique Bernard. Thermal heterogeneity within aqueous materials quantified by ^1H NMR spectroscopy: Multiparametric validation *in silico* and *in vitro*. *Journal of Magnetic Resonance*, 2018, 287, pp.56-64. 10.1016/j.jmr.2017.12.017 . hal-03527743

HAL Id: hal-03527743

<https://hal.science/hal-03527743>

Submitted on 16 Jan 2022

HAL is a multi-disciplinary open access archive for the deposit and dissemination of scientific research documents, whether they are published or not. The documents may come from teaching and research institutions in France or abroad, or from public or private research centers.

L'archive ouverte pluridisciplinaire **HAL**, est destinée au dépôt et à la diffusion de documents scientifiques de niveau recherche, publiés ou non, émanant des établissements d'enseignement et de recherche français ou étrangers, des laboratoires publics ou privés.



Distributed under a Creative Commons Attribution - NonCommercial - NoDerivatives 4.0 International License

1 Thermal heterogeneity within aqueous materials quantified by ^1H
2 NMR spectroscopy: multiparametric validation *in silico* and *in vitro*

3

4 Norbert W. Lutz^{1*}, Monique Bernard²

5

6 ^{1,2} Centre de Résonance Magnétique Biologique et Médicale, UMR 7339, Centre National de la Recher-
7 che Scientifique, Faculté de Médecine de la Timone, 27 Bd Jean Moulin, Aix-Marseille Université, F-
8 13005 Marseille, France.

9

10 ¹ Norbert.Lutz@univ-amu.fr

11 ² Monique.Bernard@univ-amu.fr

12

13 * Corresponding author

14

15

16

17

18 **Funding:** This work was supported by the Centre National de la Recherche Scientifique (CRMBM UMR 7339).

19

20

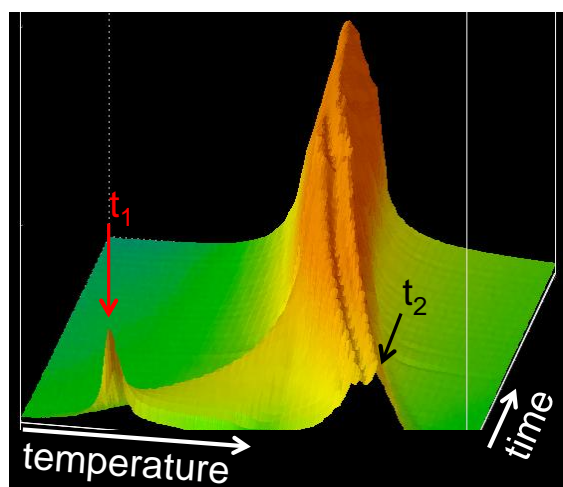
21

22 Abstract

23 We recently suggested a new paradigm for statistical analysis of thermal heterogeneity in (semi-)aqueous
24 materials by ^1H NMR spectroscopy, using water as a temperature probe. Here, we present a comprehensive *in-*
25 *silico* and *in-vitro* validation that demonstrates the ability of this new technique to provide accurate quantitative
26 parameters characterizing the statistical distribution of temperature values in a volume of (semi-)aqueous matter.
27 First, line shape parameters of numerically simulated water ^1H NMR spectra are systematically varied to study a
28 range of mathematically well-defined temperature distributions. Then, corresponding models based on measured
29 ^1H NMR spectra of agarose gel are analyzed. In addition, dedicated samples based on hydrogels or biological
30 tissue are designed to produce temperature gradients changing over time, and dynamic NMR spectroscopy is
31 employed to analyze the resulting temperature profiles at sub-second temporal resolution. Accuracy and
32 consistency of the previously introduced statistical descriptors of temperature heterogeneity are determined:
33 weighted median and mean temperature, standard deviation, temperature range, temperature mode(s), kurtosis,
34 skewness, entropy, and relative areas under temperature curves. Potential and limitations of this method for
35 quantitative analysis of thermal heterogeneity in (semi-)aqueous materials are discussed in view of prospective
36 applications in materials science as well as biology and medicine.

37

38 Graphical abstract



39

40 **Introduction**

41 We have previously presented a theoretical concept for the quantification of thermal heterogeneity in aqueous and
42 semi-aqueous materials [1]. This new method is based on statistical analyses of the ^1H NMR line shape of water,
43 a "chemical temperature probe". The new paradigm underlying our technique is grounded in the fact that (i) the
44 chemical shift of a water ^1H NMR resonance, $\delta_{\text{H}_2\text{O}}$, is a linear function of the water temperature (with a slope of
45 *ca.* 0.01 ppm/ $^{\circ}\text{C}$ [2]), and (ii) in the presence of temperature gradients, the overall water NMR line shape reflects
46 the statistical distribution of temperature values within the measured sample volume, within certain limits
47 discussed previously in detail [1]. To analyze thermal heterogeneity with this method, water ^1H NMR spectra are
48 first converted to temperature distribution curves. Then, these temperature profiles are transformed into
49 histograms by an appropriate algorithm. Based on these histograms, further mathematical algorithms developed
50 by us derive at least eight quantitative parameters (descriptors) defining the underlying temperature distribution,
51 *i.e.*, the thermal heterogeneity within the measured sample volume.

52 The specificity of our new paradigm lies in the fact that we exploit, for the first time, the entire temperature curve
53 (corresponding to an NMR line shape), to quantitatively describe a distribution of temperature values. Here, we
54 present the validation of our method for the following descriptors of temperature distribution: weighted mean and
55 weighted median temperatures [1], standard deviation, temperature range, one or multiple temperature modes (=
56 temperature curve maxima), kurtosis (peakedness [1, 3]), skewness (asymmetry [4]) and entropy (smoothness [5,
57 6]). Note that temperature skewness, kurtosis and entropy directly provide actual temperature information, akin to
58 temperature mean and standard deviation. From a statistical perspective, the latter two parameters are 1st and 2nd
59 moment descriptors, respectively, of a given (temperature) distribution, whereas skewness and kurtosis are 3rd
60 and 4th moment descriptors, respectively. In other words, skewness and kurtosis provide temperature information
61 in the same way as mean and standard deviation, albeit on a "higher level", *i.e.*, in the form of "higher moments".

62 In addition, ratios of mode heights, and ratios of areas under individual temperature modes and/or ranges are vali-
63 dated as quantitative measures of the relative sizes of volumes characterized by different temperature values. We
64 assess the validity of our method based on (i) numerically simulated water ^1H NMR spectral lines; (ii) experimen-

65 tally measured ^1H NMR spectra of well-defined aqueous test solutions and hydrogels (agarose gels [7]); (iii) dy-
66 namic ^1H NMR spectroscopy of hydrogels in the presence of temperature gradients changing over time, using a
67 dedicated experimental design; and (iv) *in-vitro* ^1H NMR experiments on biological tissue.

68 Our simulations are entirely unrelated to conventional NMR lineshape simulations based on spin dynamics or
69 Bloch equations. The purpose of our numerical simulations is to examine the following questions: 1) How are the
70 quantitative descriptors of statistical temperature distribution obtained through our algorithm interpreted in terms
71 of distribution curve properties? 2) What are the ranges of the statistical descriptor values for distribution curves
72 to be expected from actual experiments? 3) How sensitive are the resulting temperature distribution curves, and
73 their associated descriptor values, to actual temperature gradients *vs.* spurious effects, *i.e.*, curve shape contribu-
74 tions unrelated to temperature distribution? 4) What are the effects of water ^1H NMR line shape correction by our
75 empirical deconvolution method on the resulting distribution curve shapes and, consequently, on the derived de-
76 scriptors of temperature profiles? 5) How do temperature distribution descriptors derived from simulated spectra
77 compare with those from measured NMR spectra? Thus, our simulations do not serve to elucidate NMR physics,
78 but to study temperature distributions, albeit derived from water NMR resonances.

79 All calculations are performed employing the preprogrammed EXCEL spreadsheet provided in our previously
80 published paper [1]. We also investigate how temperature profile measurements can be used to efficiently and
81 quantitatively study dynamic phenomena such as heat transfer and thermal conduction, as water ^1H NMR spectra
82 can be acquired with sub-second temporal resolution. Our findings for basic hydrogels and biological samples
83 have significant implications for studying the relationship between temperature variations and other physical,
84 chemical and biological properties in a variety of (semi-)aqueous materials. A broad scope of research ranging
85 from materials science and physical chemistry of soft matter to biology and medicine [8-11] may benefit from our
86 approach.

87

88

89 **Results and Discussion**

90 The most relevant results of our study are presented in this section. Additional data are included in the Results
91 section of S1 Supplemental Materials 1 that also comprises Figs. S-1 through S-29, and in S2 Supplemental
92 Materials 2 with Figures S-30 through S-45 and Tables S-1 through S-5. Taken together, the values given in our
93 tables indicate the ranges to be expected for statistical descriptors in experimental distribution curves.

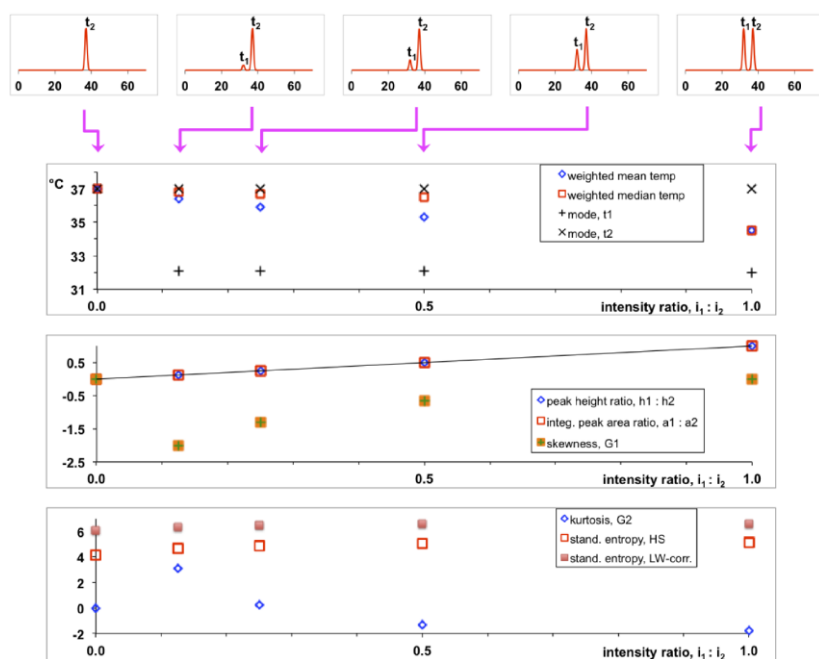
94
95

96 **Studies of unimodal, bimodal and trimodal temperature profiles - overview**

97 When subjected to a heating or cooling process, most materials are likely to experience irregularly shaped internal
98 temperature distributions, due to thermal gradients that are more or less continuous and variable over time.
99 However, for the purpose of validating our method we initially focused on numerically simulated unimodal,
100 bimodal and trimodal temperature distributions, because the concept of quantitative parameters of thermal
101 heterogeneity is best tested and verified on the basis of models representing well-defined temperature distribution
102 functions [1]. In fact, most quantitative parameters suggested in this report are universally applicable to any given
103 distribution of temperature values; their use does not depend on the existence of distinct temperature modes. Our
104 first *in-silico* validations were based on temperature modes at $t_1 = 32.0$, $t_2 = 34.5$ or $t_3 = 37.0$ °C (Table 1, for
105 simulated Gaussian spectral lines at 11.7 T). Different bimodal (or trimodal) temperature distributions were
106 modeled by varying the relative intensities or amplitudes i_1 (or i_1 and i_2) of 32.0 °C (or 32.0 and 34.5 °C) modes,
107 added to an i_2 (or i_3) 37.0 °C mode. Subsequently, statistical descriptors were derived for unimodal (Table 1,
108 column A), bimodal (columns B through E) and trimodal (columns F through I) temperature distributions, as a
109 function of the relative mode intensities characterizing each distribution. For the unimodal and bimodal
110 distributions of this series, the relative intensities of the 32 °C vs. 37 °C modes were used to scale the abscissae of
111 the diagrams in Fig. 1. Analogous validations were performed for simulated Gaussian spectral lines at 3 T (Table
112 S-1 and Fig. S-2); and for simulated Lorentzian spectral lines at 11.7 T (Table S-2 and Fig. S-3) and 3 T (Table S-
113 3 and Fig. S-4). These and similar temperature distributions based on measured ^1H NMR spectra are discussed in
114 S1 Supplemental Materials 1.

115 Quantification of oligomodal temperature distributions

116 We have previously shown that under high-field conditions, up to three distinct regions of similar size can be
117 identified based on differing temperature values, within a temperature range close to 5 °C (no assumptions are
118 made with respect to the size and spectral distribution of the underlying sample volume elements) [1]. This
119 finding takes into account that any experimentally obtained NMR resonance has a finite linewidth even in the
120 absence of any temperature gradient, essentially due to T_2 and T_2^* effects [1]. In the absence of such spurious
121 effects, our simulated uni, bi and trimodal temperature distribution curves, and the associated spectra, would have
122 the shape of one, two or three delta functions, respectively. The influence that removing these spurious effects has
123 on statistical descriptors of temperature distributions is discussed in S1 Supplemental Materials 1. In the
124 following, we focus on "raw" lineshapes, *i.e.*, before any correction for spurious effects.



125

126 **Figure 1.** Temperature distributions as a function of relative contributions of mode 1 ($t_1 = 32^\circ\text{C}$) and mode 2 ($t_2 =$
127 37°C), based on numerically simulated Gaussian water ^1H NMR resonances (line width, 7.5 Hz) for a high-field
128 magnet (11.7 T). Top row: temperature distribution curves (= temperature profiles). Second to fourth rows:
129 changes in statistical descriptors of temperature distributions with increasing mode 1 contribution (see also Table
130 1).

131

132

133 In our simulated oligomodal curves, the corresponding mode areas may strongly overlap. The implications of this
134 situation for temperature profile quantitation will be discussed in the following. Changes of quantitative
135 temperature distribution descriptors as a function of the shape of bimodal temperature profiles are best visualized
136 by diagrams plotting descriptor values against increasing contribution of mode t_1 to a distribution dominated by
137 mode t_2 , as indicated by increasing intensity ratios, $i_1:i_2$ (Fig. 1, Figs. S-2 through S-4 for simulated, and Figs. S-5
138 and S-42 for measurement-based distributions). For distributions derived from high-field spectra, t_1 and t_2 were
139 rather stable because peak overlap was negligible for a difference of 5 °C (Figs. 1 and S-3 for simulated, and Figs.
140 S-5 and S-42 for measured distributions). By contrast, the relatively broad lines derived from simulated low-field
141 spectra resulted in high-temperature mode values decreasing, and in low-temperature mode values increasing
142 with increasing contribution of mode t_1 (Figs. S-2 and S-4). In many cases, the temperature of the less intense
143 mode, t_1 , could only be estimated, notably for $i_1:i_2 = 0.125$ and 0.25 . As was to be expected for left-skewed
144 distributions, $\overline{\text{temp}} < \widetilde{\text{temp}}$ for $i_1:i_2 = 0.125, 0.25$ and 0.5 . For $i_1:i_2 = 1.0$, only simulated distributions were
145 perfectly symmetric and, therefore, yielded identical values for, $\overline{\text{temp}}$ and $\widetilde{\text{temp}}$, whereas measured distributions
146 were slightly right-skewed due to an increased right foot (or tail) of the underlying NMR resonances (spurious
147 effect due to magnetic-field inhomogeneity). This resulted in somewhat smaller values for $\widetilde{\text{temp}}$ vs. $\overline{\text{temp}}$ (Figs.
148 S-5 and S-42). In summary, mode errors were small but not entirely negligible for modes of small intensity
149 located very close to one or two modes of much larger intensity. Since our simulation predicted rather poor
150 resolution for low-field spectra, we decided not to acquire experimental low-field NMR spectra.

151 The concepts of skewness, kurtosis and entropy are generally employed to characterize unimodal probability
152 distributions [12]. However, they can also reveal global characteristics of temperature profiles with more than one
153 mode [1]. For instance, the symmetric distributions formed by two identical, simulated high-field resonances
154 displayed in Figs. 1 and S-3 (top right curves) result in (nearly) zero skewness (Tables 1 and S-2, columns B).
155 Also the less ideal, but theoretically symmetric temperature profiles based on two identical resonances, simulated
156 for low field (Figs. S-2 and S-4, top right curves) or measured (Figs. S-5 and S-42, top right curves) had very low
157 absolute skewness values (Tables S-1, S-3 through S-5, columns B). Predictably, skewness values [1] of bimodal

158 distributions continuously increased with $i_1:i_2$ increasing from 0.125 to 1.0, *i.e.*, with decreasing asymmetry as
159 indicated by modes of unequal peak heights. Due to the relatively broad bases of Lorentzians, the symmetry of
160 Lorentzian distributions is less influenced by the difference in heights between the two modes, than are Gaussian
161 distributions. This is reflected by (i) relatively low absolute skewness values, and (ii) relatively small increases in
162 skewness with $i_1:i_2$ increasing from 0.125 to 1.0 for high-field Lorentzians *vs.* Gaussians. However, in low-field
163 spectra, the bases of Gaussians also become relatively broad, which approaches the skewness behavior of
164 Gaussians to that of Lorentzians. Kurtosis continuously decreased over the same range of $i_1:i_2$ values, notably for
165 distributions composed of narrow peaks, because the overall distribution becomes less peaked with increasing t_1
166 contribution. More generally, distributions made up of broad and, therefore, strongly overlapping mode areas vary
167 little in shape with increasing $i_1:i_2$ ratio; therefore, quantitative descriptors of curve shape also show relatively
168 little change, although there was a drastic difference between the kurtosis values of a single narrow Gaussian (G_2
169 = 0, Fig. 1) and a single narrow Lorentzian ($G_2 = 14$, Fig. S-3). In summary, the skewness, kurtosis and entropy
170 values of our bimodal curves can be readily interpreted in accordance with the underlying line shapes [1].

171 For trimodal distributions with modes in 2.5 °C intervals, mode temperature values (t_1 , t_2 and t_3) did not change
172 with intensity ratios, $i_1:i_2:i_3$, when simulated high-field Gaussians were compared (Table 1, columns F - I). Very
173 small variations (by *ca.* 0.1 °C) with intensity ratios were observed for measured high-field (near-)Gaussians
174 (Table S-4, columns F - I), and for simulated high-field Lorentzians (Table S-2, columns F - I). For the remaining
175 trimodal distributions tested, the resolution was often insufficient to determine the exact value, or even the
176 presence, of all three modes. This confirms for trimodal distributions the same conclusions presented above for
177 bimodal distributions, namely that working under high-resolution conditions (high magnetic fields, (near-)
178 Gaussian line shapes) is essential for obtaining spectra with highest sensitivity to temperature gradients, and for
179 minimizing spurious effects on temperature profiles. Unlike our bimodal distributions, trimodal distributions have
180 not been generated by systematically varying only one specific intensity parameter value such as $i_1:i_2$, since the
181 focus here was on providing examples for qualitatively different curve shapes. Nonetheless, there was a global
182

Table 1. Statistical parameters characterizing simulated temperature

heterogeneities.

descriptor	A	B	C	D	E
weighted mean, $\overline{\text{temp}}$ [°C]	37.0	34.5	35.3	35.9	36.4
weighted median, $\widetilde{\text{temp}}$ [°C]	37.0	34.5	36.5	36.7	36.8
mode, t_1 [°C]	n/a	32.0	32.1	32.1	32.1
mode, t_2 [°C]	37.0	37.0	37.0	37.0	37.0
peak area ratios ($a_1:a_2$)					
- integrated	n/a	1.00:1	0.50:1	0.25:1	0.13:1
- theoretical	n/a	1.00:1	0.50:1	0.25:1	0.125:1
peak height ratios ($h_1:h_2$)	n/a	1.00:1	0.50:1	0.25:1	0.125:1
skewness, G1	0.000	0.000	-0.6	-1.314	-2.009
kurtosis, G2	0.000	-1.795	-1.319	0.210	3.124
standard entropy, H_S	4.13	5.13	5.05	4.86	4.64
	[6.10]	[6.64]	[6.59]	[6.47]	[6.35]

183

descriptor	F	G	H	I
weighted mean, $\overline{\text{temp}}$ [°C]	34.5	35.2	35.5	35.8
weighted median, $\widetilde{\text{temp}}$ [°C]	34.5	36.2	36.2	36.4
mode, t_1 [°C]	32.1	32.1	32.1	32.2
mode, t_2 [°C]	34.6	34.6	34.6	34.6
mode, t_3 [°C]	37.0	37.0	37.0	37.0
peak area ratios ($a_1:a_2:a_3$)				
- integrated	1.00:0.99:1	0.51:0.24:1	0.25:0.50:1	0.12:0.50:1
- theoretical	1.00:1.00:1	0.50:0.25:1	0.25:0.50:1	0.125:0.50:1
peak height ratios ($h_1:h_2:h_3$)	1.00:1.00:1	0.50:0.25:1	0.25:0.50:1	0.12:0.50:1
skewness, G1	-0.031	-0.541	-0.767	-0.891
kurtosis, G2	-1.266	-1.238	-0.439	0.125
standard entropy, H_S	5.63	5.45	5.43	5.30
	[6.51]	[6.55]	[6.44]	[6.37]

184

185 Data are based on Gaussian lineshapes, corresponding to ^1H NMR resonances at 11.7 T. A, single Gaussian, 37°C; B-E: two186 Gaussians, 32°C and 37°C; B, equal intensities; C, intensity ratio $i_1:i_2 = 1:2$; D, intensity ratio $i_1:i_2 = 1:4$; E, intensity ratio187 $i_1:i_2 = 1:8$; F-I: three Gaussians, 32°C, 34.5°C and 37°C; F: equal intensities; G, intensity ratio $i_1:i_2:i_3 = 2:1:4$; H, intensity188 ratio $i_1:i_2:i_3 = 1:2:4$; I, intensity ratio $i_1:i_2:i_3 = 1:4:8$. Entropy values given in [] are based on peaks simulated for the same189 linewidth (in ppm) as for 3 T (Table S-1). a_n , h_n and i_n : areas, peak heights and intensities, respectively, associated with190 modes t_n , with $n = 1$ to 3.

191

192

193 trend toward stronger left skew and increased kurtosis from column F to column I (Table 1, simulated high-field
194 Gaussians). This reflects the gradual transition from a rather symmetric and flat temperature profile with equal
195 mode intensities ($i_1=i_2=i_3$), to a more asymmetric and peaked profile with intensities strongly increasing from
196 lower to higher temperatures ($i_1<i_2<i_3$). As a consequence, the overall temperature distribution curve increasingly
197 takes on the shape of a steep slope (see Fig. S-6, bottom row, for visualization of intensity ratios used in all
198 Tables, and in Figs. S-6 and S-43). Trimodal distributions composed of Lorentzian, low-field and experimental
199 temperature modes, exhibited skewness and kurtosis trends that corresponded to those observed for high-field
200 Gaussian temperature modes, but less consistently so. Obviously, the increased overlap between mode areas,
201 caused by broader bases in all three modes, modified the characteristics of temperature distributions significantly.
202 As opposed to skewness and kurtosis, standard entropy only exhibited relatively small variations within any given
203 series of mode intensity variations. However, there were consistent differences between series, *i.e.*, between
204 distributions based on high-field and low-field NMR spectra, and between distributions based on Gaussian and
205 Lorentzian-like areas under the modes. This finding underlines the validity and the complementary character of
206 the statistical descriptors of temperature distributions used in this work. These and further results for multimodal
207 temperature distributions are presented in more detail in S1 Supplemental Materials 1.

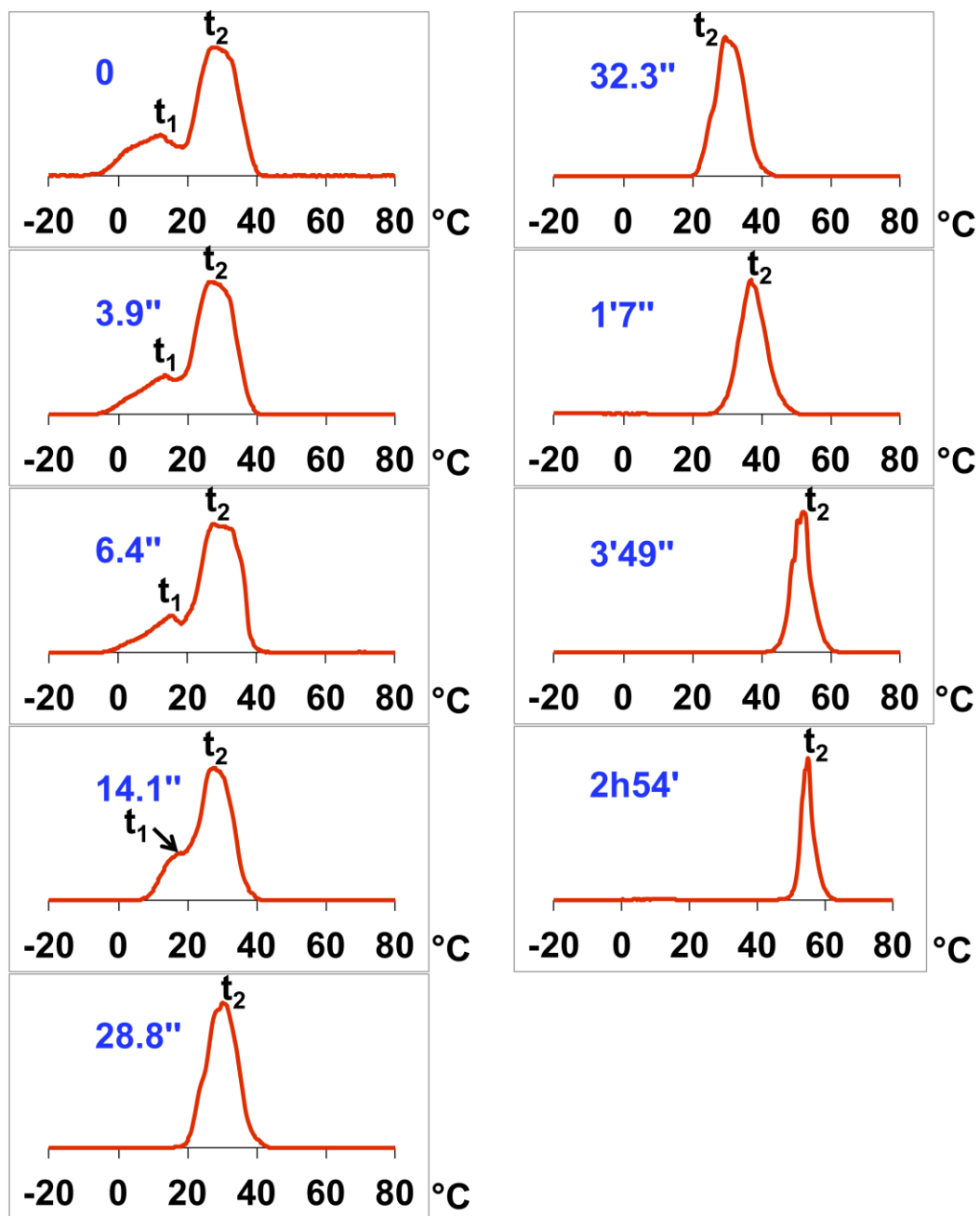
208

209 **Effects of global vs. local heat exchange in gel phantoms**

210 The first experiment with a dedicated temperature gradient sample (gel phantom) was performed as presented in
211 Figure S-41 a. Before insertion of the narrow tube into the wide tube, the former was brought to about -15 °C, and
212 the latter to about 60 °C (Fig. S-40 a, blue and red broken lines, respectively). The delays needed to remove the
213 tubes from their respective preheating/precooling environments (*ca.* 3 s), dry and assemble the tubes (*ca.* 20 s)
214 and lower them into the NMR probe (8-10 s), resulted in significant heat exchange (i) between the NMR tubes
215 and the surrounding air, and (ii) between the two phantom compartments, even *before* the first spectrum was
216 measured. For this reason, the first temperature profile exhibited two broad, partially overlapping mode areas,

217 instead of two narrow, well-separated mode areas, thus mimicking an irregularly shaped temperature distribution
218 which may occur in many real-life situations of rapid sample heating or cooling. [Note that particular NMR
219 singlets with temperature-invariant chemical shifts, used as chemical-shift references, were obtained
220 simultaneously with the water resonances, and from the same sample volumes. These singlets were constant,
221 narrow and regularly shaped, as was to be expected. See S1 Supplemental Materials 1 for details.] The high-
222 temperature mode was below, and the low-temperature above the starting temperature of the respective individual
223 tube. The behavior of the temperature profile was followed over a period of *ca.* 3 h, with increasing time intervals
224 between measurements. The lists of intervals for all relevant experiments are given in S1 Supplemental Lists.
225 Five of a total of 146 subsequent measurements performed in this series were selected to document the most
226 significant changes in curve shape occurring over time (Fig. S-40 a - e, height-normalized profiles; see also Fig.
227 2). In the initial phase of these measurements, the two mode areas progressively merged to form one unimodal,
228 broad temperature distribution curve (Fig. S-40 a - c).

229 Subsequently, the line width of the resulting curve decreased over time, and the temperature mode asymptotically
230 approached *ca.* 60 °C. The emergence of a uniform, stable temperature throughout the gel phantom was imposed
231 by a temperature-regulated gas stream (Fig. S-41 a). These results can be explained by a combination of local and
232 global heat exchange. The initially observed thermal equilibration is the result of heat exchange between the two
233 phantom compartments (= local effect), as is the subsequent narrowing of the curve. By contrast, the fact that the
234 phantom temperature progressively approached the final temperature of about 60 °C is owed to heat exchange
235 with the surrounding gas stream, influencing and, ultimately, determining the temperature of both inner and outer
236 tubes (= global effect). Obviously, both effects were not strictly separated in time as the sample heating by the gas
237 stream must have started as soon as the phantom was exposed to the gas stream. However, local heat exchange
238 initially dominated and was responsible for the early, major changes in the temperature profile, while the
239 subsequent drift of the overall sample temperature to high values was caused by the then dominating global heat
240 exchange with the gas stream. Note that the curve shapes discussed above are based on NMR spectra processed
241 with Lorentzian filtering (1-Hz apodization). Alternative filtering parameter values and methods can slightly
242 modify details of curve shapes, as discussed in S1 Supplemental Materials 1.



244

245 **Figure 2.** Selected height-normalized temperature profiles (with delays after first measured profile) obtained from
 246 a series of high-field (9.4 T) NMR measurements on the temperature heterogeneity phantom shown in Fig. S-41.
 247 Apodization with LB = 1 Hz, followed by enhanced baseline correction.

248

249

250

251 The general behavior of our phantom design was confirmed by quantitative evaluation as described in the
252 following paragraphs. Results from the above experiment are shown in Figure 2 (height-normalized curve shapes)
253 and Figure 3 (values of descriptors of thermal heterogeneity). Both figures present data for the same time points,
254 in the same measurement series. Until 14.1 s after the first measurement, there was little change in weighted mean
255 temperature and almost no change in median temperature (Fig. 3, top left), suggesting very little net heat
256 exchange between the phantom as a whole and its environment (gas stream). After 32.3 s, mean and median
257 temperatures increased in a sigmoidal fashion, approaching the final temperature (see S1 Supplemental Materials
258 1 for the choice of time points). At 14.1 s following the first measurement, the low and high-temperature mode
259 areas began to merge (Fig. 2), and at 28.8 s only one mode (= global temperature maximum; Fig. 3, bottom left)
260 was distinguishable. Interestingly, neither entropy nor kurtosis changed uniformly over time (Fig. 3, top right).
261 Kurtosis reached a moderately pronounced maximum when the two modes were still clearly identifiable (6.4 s),
262 then went through a minimum at 14.1 s (before complete merger of the mode areas), followed by an increase as
263 the temperature distribution curve became very narrow (partial Lorentzian character). This behavior is linked to
264 the well-known fact that kurtosis can increase as a consequence of two different influences: either due to tails
265 extending far from the mode (6.4 s, left tail, Fig. 2), or due to a peak top that is narrow compared to the tails (end
266 of series: 2h54m). Two phases can be identified in the temporal behavior of skewness: an almost constant,
267 moderate left skew as long as the two modes were still clearly distinguishable (6.4 s), then a slow increase up to a
268 slightly positive value for the final narrow curve, but still close to symmetry ($G1 = 0$). Thus, quantifying both
269 skewness and kurtosis permits a more detailed description of the changing temperature profile than would be
270 possible by simply using mean, median and mode temperature values. Range and standard deviation also changed
271 in a biphasic fashion, albeit in a more uniform way, with inflection points close to the point of complete merger of
272 the mode areas (between 14.1 and 28.8 s). As was to be expected, peak height ratios and peak area ratios reflected
273 the relative decrease in t_1 mode area vs. t_2 mode area (a_1 vs. a_2) during the early phase of the experiment, where
274 heat exchange between phantom compartments is dominating (Fig. 3, bottom right). As a result, the combination
275 of multiple statistical descriptors of temperature heterogeneity was able to give a detailed quantitative view of the
276 heat exchange processes occurring over time.

277 We complemented this analysis with an overview "at a glance", enabling easy visualization of the evolution of all
278 temperature profiles over the entire period of serial measurements. This was achieved by plotting all profiles
279 together as a stacked plot (Fig. 4 a), and connecting the individual profiles as to generate a virtual three-
280 dimensional surface plot (Fig. 4 b). Top projections of this surface plot give an immediate impression of the time
281 course of the underlying temperature distributions (Fig. 4, c - e). However, it is also very instructive to view the
282 three-dimensional shape of the entire surface plot from different angles. This is achieved by rotating the virtual
283 three-dimensional object on a computer screen (S1 Horizontal rotation of 3D temperature profiles, and S2 Vertical
284 rotation of 3D temperature profiles), thus fully exploiting the fact that the surface plot is assembled of a series of
285 complete temperature profiles. Horizontal rotation by 360° (Video S-1), and vertical rotation by 90° from front
286 view to top projection (Video S-2) can be performed under manual control by using the video scrollbar. Close
287 inspection reveals that, for instance, temperature modes appear as "mountain ridges" in these pseudo-3D
288 renderings. Following the appearance and disappearance of this and other 3D structural features as a function of
289 measurement time provides additional insight into the dynamics of thermal processes in the material of interest.
290 Note that in these videos, as in Fig. 4 a and b, narrow temperature profiles appear significantly higher than broad
291 profiles, which is a consequence of using area normalization (for details see S1 Supplemental Materials 1).
292

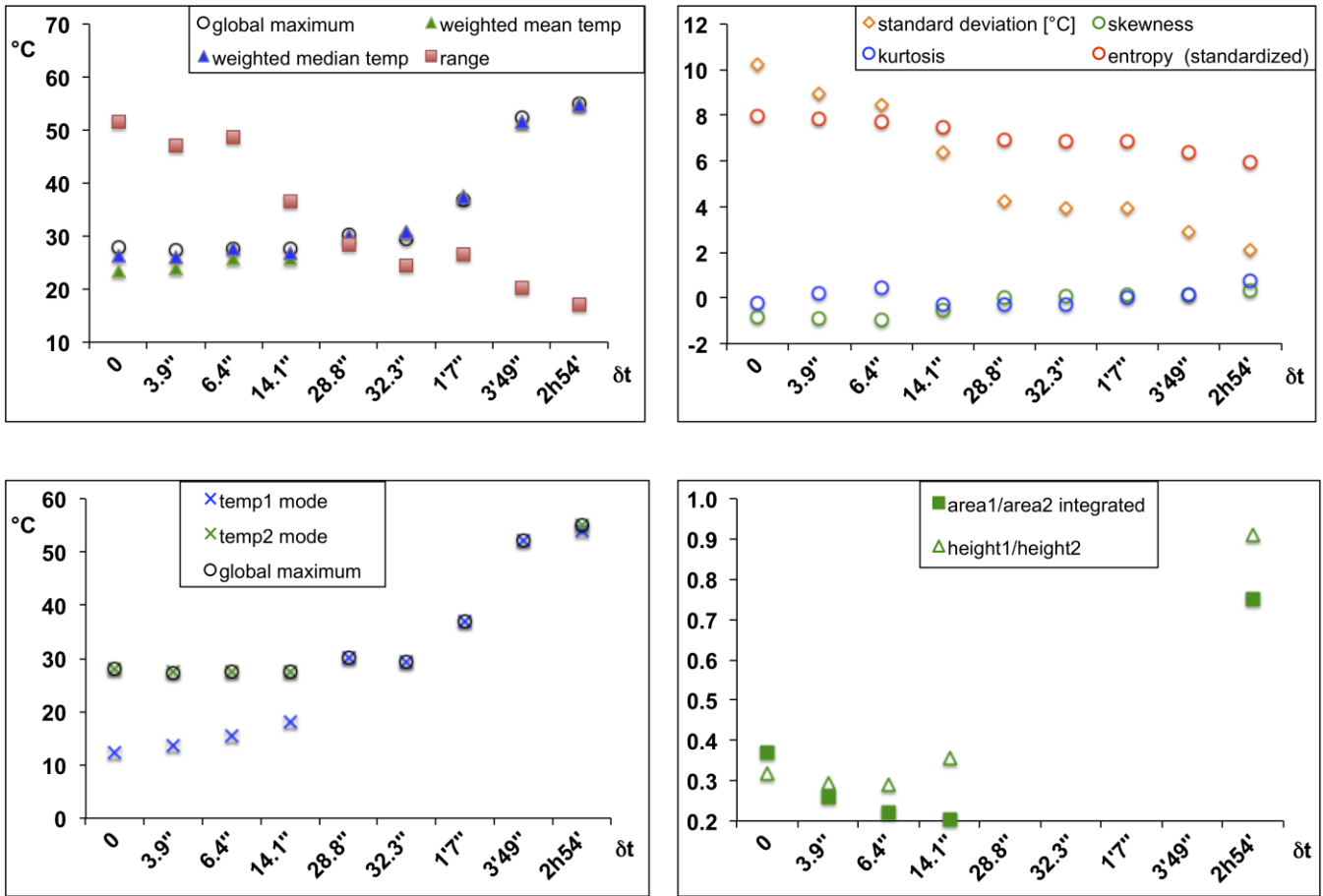


Figure 3. Descriptors of temperature heterogeneity calculated from temperature profiles presented in Fig. 2.

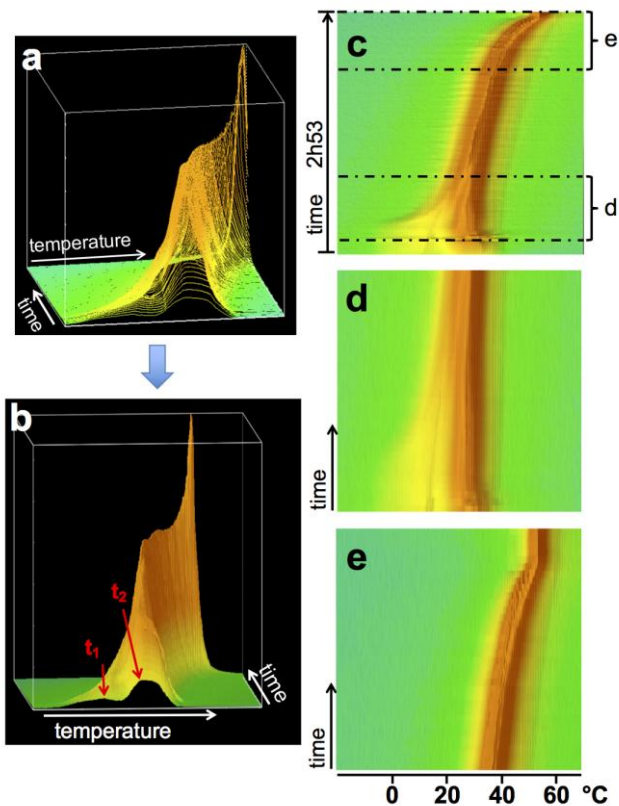


Figure 4. Generation of surface plots by combining all 136 temperature profiles (2 h 53 min starting from the first measurable distribution curve) determined in the experimental series underlying Fig. 2. a: superimposed area-normalized temperature profiles, oblique view; b: surface plot obtained from (a) by generating a closed surface over all temperature profiles; c: same surface plot as (b), represented as top projection; d and e: vertically enlarged portions of (c), as annotated and defined by dashed lines in (c).

In addition to the example of thermal equilibration accompanied by global heating discussed above, we studied three more cases of dynamic heat exchange according to the protocol shown in Fig. S-41 a: (i) for a phantom consisting of gel-filled compartments of the same starting temperatures as described above (-15 and 60 °C), exposed to a cold (*ca.* -4 °C) N₂ stream during measurement; (ii) as (i), but phantom compartments with identical starting temperatures (60 °C); and (iii) as (ii), but room-temperature (21 °C) environment for sample during NMR

experiment, without gas flow. In summary, results obtained in well-defined phantom experiments are readily explained by the experimental conditions chosen, supporting the validity of the approach suggested in this work. The first of these experiments (phantom with internal temperature gradient and external cooling) demonstrated, for the case of external cooling (i), biphasic thermal behavior similar to that observed for the analogous heating experiment described in the preceding paragraphs. Comparisons between passive and active cooling showed that the efficiency of heat exchange between phantom and environment can be monitored by measuring associated variations in parameters describing temperature distribution curves. These examples are presented in more detail in S1 Supplemental Materials 1.

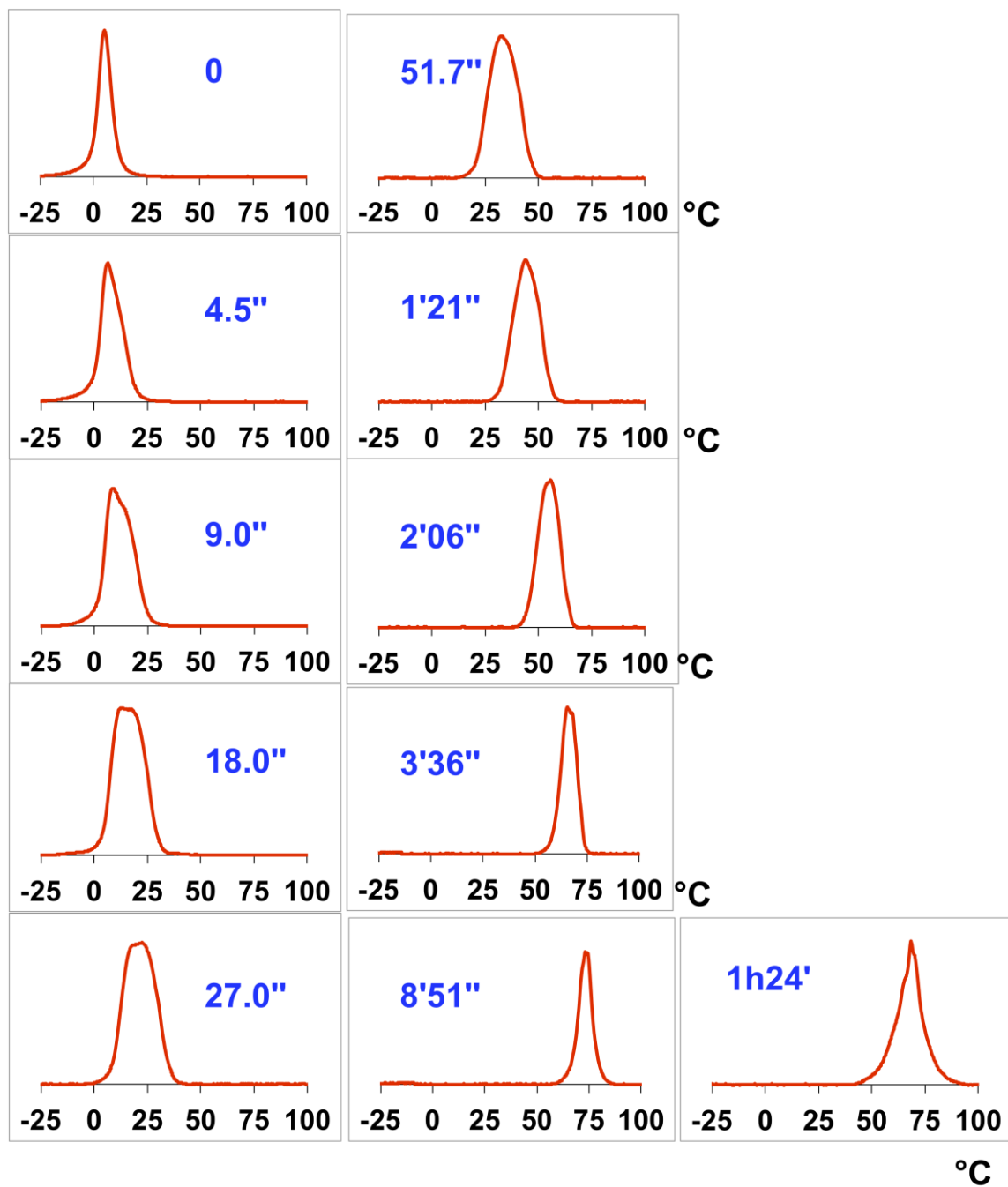


Figure 5. Selected height-normalized temperature profiles (with delays after first measured profile) obtained from a series of high-field (9.4 T) water ^1H NMR measurements on bovine muscle tissue, contained in a 10-mm diameter tube being heated from *ca.* 0 to > 70 °C during measurement by way of an external stream of temperature-regulated nitrogen.

Effects of heat exchange in biological tissue

Prompted by previously published findings that the temperature dependence of water chemical shift (0.01 ppm per °C, [1]) is virtually identical for aqueous solutions and biological tissue, we decided to test the congruence of the results obtainable for bovine muscle tissue as a model for mammalian tissue, with those obtained above for hydrogels. Bovine muscle tissue that was initially at thermal equilibrium, was first measured being externally cooled from 45 to *ca.* 0 °C, then being heated from 0 °C to 80 °C by analogy with the gel experiments mentioned above. Due to the relatively small temperature gradients generated during the cooling period, changes in line shape were very minor. By contrast, line shape alterations were readily discernable for the heating period (Fig. 5) where the initial difference between sample temperature (*ca.* 0 °C) and N₂ stream (80 °C) caused marked temperature gradients across the sample. These gradients even resulted in two discernible, albeit heavily overlapping, modes for 9 to 27 s after the first measurement (Fig. S-34). Note that at the end of the experiment, the muscle tissue structure degraded due to heat exposure. At this time, we decided to reduce the N₂ stream temperature to 60 °C. This resulted in an atypically broad line shape and a slightly reduced measured sample temperature (Figs. 5 and S-34, last time points). This return to somewhat lower temperatures can also be seen in the corresponding surface plot (Fig. S-35 d). It is obvious that temperature range and standard deviation exhibit a broad maximum at 18 s after the first measurement (Fig. S-34), corresponding to the largest line width (Fig. 5). However, the temperature distribution remained rather symmetric throughout the measurement series; this is reflected by the fact that mean \approx median \approx mode(s) \approx global maximum temperature, and that skewness values are close to zero (at start of series: small and decreasing left skew) [1]. Kurtosis was highest for the first measurement, where lines were very narrow (limit of zero temperature gradient). The decreasing values for peak area and height values are consistent with a globally increasing temperature. The qualitatively similar behavior of biological tissue and gel phantoms hints at the possibility to apply our method to *in-vivo* measurement in future projects.

Conclusion

The first concept for measuring statistical distributions of temperature values in aqueous materials, whose theoretical basis had been provided previously, has been validated in a comprehensive study. The following quantitative descriptors of thermal heterogeneity were successfully evaluated by numerical simulation (*in-silico* experiments) and water proton NMR spectroscopy (*in-vitro* experiments): temperature means, medians, modes, ranges and standard deviations; skewness, kurtosis and entropy; as well as ratios of peak heights and areas under temperature distribution curves. The algorithms underlying our new method are now confirmed for uni-, bi- and trimodal temperature distributions. We further demonstrated that the dynamics of statistical temperature distribution during heat exchange processes in hydrogel can be characterized quantitatively by analyzing the associated temperature profiles at sub-second time resolution. We also confirmed the applicability of our approach to biological materials (muscle tissue).

Fast data acquisition has the added advantage of providing far more realistic temperature snapshots than other, notably image-based, methods based on water proton chemical shift such as MRSI-PRF (magnetic resonance spectroscopic imaging - proton resonance frequency), as the latter methods require far more time for data collection. In the presence of thermal gradients, diffusing water molecules provide a mechanism for thermal equilibration, causing changes in the temperature profile over the data acquisition time. Thus, temperature profiles are "smeared out" across the temperature ranges concerned. In our method, "smearing" takes place over a much smaller time period (a few 100 ms) than it does in the currently available image-based experiments mentioned above. For instance, in MRSI-PRF data acquisition occurs over *ca.* 10 s per slice, and becomes much longer for an entire volume.

To visualize and guide these analyses, we constructed virtual 3D plots complemented by examples of virtual 3D videos for close inspection of changes in temperature profiles over time. The suggested approach provided consistent and robust results for temperature ranges down to a few degrees Celsius. For very small ranges, the

deconvolution-based curve shape correction concept previously introduced by us was validated for an *in-silico* model of an asymmetric temperature distribution.

Future perspectives include full implementation and evaluation of our deconvolution method for compensating spurious influences on temperature profiles, and its adjustment to temperature-dependent response functions. Potential applications of our suggested method concern a broad range of aqueous materials used in various disciplines, such as investigations of the formation and alterations of hydrogels and similar aqueous materials currently being developed in materials science. Furthermore, research and development in food science, quality control for industrial purposes, and biomedical procedures such as *in-vivo* examination of tissue properties may be of particular interest for our method [8-11], notably in the context of tumor treatment by hyperthermia (*e.g.*, thermoablation) or cryotherapy, and other processes involving major perturbations of temperature regulation. Caution should be exercised if our technique is to be applied to special materials such as hydrated solids, *e.g.*, porous materials loaded with water. Since our method has been developed for typical aqueous materials, it does not currently account for situations characterized by a nonlinear relationship between water ^1H chemical shift and temperature. However, the latter condition may be accommodated by future developments based on our approach.

Methods

In this section, the *in-silico* and *in-vitro* procedures employed in the validation of our new approach are described; additional technical details are presented in the Methods section of S1 Supplemental Materials 1.

***In-silico* calculations**

The purpose of our *in-silico* calculations was twofold: (i) to study statistical descriptors characterizing the overall temperature distributions resulting from the addition, in varying proportions, of up to three simulated temperature curves, and (ii) to enable quantitative comparisons between heterogeneity parameter values derived from models of theoretical (*i.e.*, simulated) and measured temperature distributions. A range of well-defined temperature distributions were computer simulated to calculate at least eight descriptors for each of these distributions [1]. The temperature distributions investigated were chosen as to represent different degrees of heterogeneity; they

range from narrow (very homogeneous) distributions about a single mode (= dominating temperature value) to broad (very heterogeneous) distributions about up to three modes of varying intensities. The temperatures studied in our *in-silico* examples lied between 32 to 37 °C; however, due to the linearity between $\rho_{\text{H}_2\text{O}}$ and temperature, distribution patterns are invariant to shifts on the absolute temperature scale. Further specifics on the rationale [13-17] for the choice of our *in-silico* parameters are given in S1 Supplemental Materials 1.

Acquisition of ^1H NMR spectra

Gel phantoms for temperature gradients

Combined test samples designed to provide genuine temperature gradients, herein called phantoms, were generated as follows. An alkaline (pH 8.2) gel sample containing 1 % agarose and 80 mM PCho was heated to about 90 °C and filled into a 5-mm NMR tube which was then put on ice. In addition, an alkaline gel sample containing 1 % agarose and 80 mM NAA was heated to about 90 °C and filled into a 10-mm NMR tube, which was then maintained at 60 °C in a water bath. Subsequently, the heated 10-mm tube was removed from the water bath, and the cooled 5-mm NMR tube was immediately inserted into the 10-mm tube, upon which the combined phantom was quickly lowered into a 10-mm NMR probe. Simultaneously, a series of ^1H NMR experiments was started by way of home-made AU programs (Bruker macros based on the C programming language; see Appendix in S1 Supplemental Materials 1). These experiments consisted of pulse-acquisition sequences [18] executed in increasing intervals ranging from 0.82 s to > 1 h. In the NMR probe, the sample was actively heated by a 60 °C, or cooled by a 0 °C nitrogen stream, respectively, during the entire series of NMR sequences (Fig. S-41 a). The experiment was repeated with both tubes being heated together to about 90 °C (Fig. S-41, top right) and adjusted to 60 °C before starting NMR acquisitions as described above. During these NMR experiments, the sample was either kept in the probe initially adjusted to room temperature (Fig. S-41 a), without sample spinning or temperature regulation; or was actively cooled by a 0 °C nitrogen stream. In a fifth series of phantom measurements, the 5-mm NMR tube was inserted into the 10-mm NMR tube shortly *after* the start of data acquisition (Fig. S-41 b; NMR experiments as in preceding experiments, except for minimum delay of 0.41 ms

between two subsequent spectrum acquisitions). This experimental design was suitable for close inspection of the fast temperature gradient changes occurring immediately after the combination of high and low-temperature gels in the phantom.

Test samples consisting of biological tissue

To demonstrate the applicability of our approach to mammalian tissue, we have designed a test sample consisting of bovine muscle tissue (lean veal). Tissue was cut into small pieces that were progressively transferred to a 10-mm NMR tube partially filled with phosphate buffered saline (pH 7.2). Occasional air bubbles were removed by moving the pieces of tissue in the buffer solution. After each addition, tissue was pushed to the bottom of the tube by exerting vertical pressure to minimize any space between tissue pieces, and between tissue and the wall of the tube. Once the available space was filled with muscle tissue to a height of 1-2 cm above the sensitive volume of the probe, the supernatant buffer solution was removed with a pipette. This procedure ensured that nearly all the material in the sensitive volume consisted of muscle tissue, and that the residual buffer volume was no more than a few percent of the total volume. The filled NMR tube was brought to *ca.* 40 °C in a water bath. ¹H NMR spectra were acquired according to the protocols described in the preceding paragraph for temperature gradient gel phantoms, first for temp_{nom} progressively decreasing to 278 K, then progressively increasing from 278 K to 340 K. See S1 Supplemental Materials 1 and our preceding paper [1] for further details concerning acquisition, processing and post-processing of ¹H NMR spectra [19, 20].

References

1. Lutz NW, Bernard M. Multiparametric Quantification of thermal heterogeneity within aqueous materials by water 1H NMR spectroscopy: Paradigms and Algorithms. PLOS ONE. 2017; 12(5), e0178431.
2. Muller N, Reiter RC. Temperature dependence of chemical shifts of protons in hydrogen bonds. J Chem Phys. 1965;42:3265-9.
3. Sokal RR, Rohlf FJ. Biometry. 3rd ed. New York: Freeman; 1995.

4. Doane DP, Seward LE. Measuring Skewness: A Forgotten Statistic? *J Stat Educ.* 2011;19(2):1-18.
5. Cover TM, Thomas JA. *Elements of information theory.* New York: Wiley; 1991.
6. Lesne A. Shannon entropy: a rigorous notion at the crossroads between probability, information theory, dynamical systems and statistical physics. *Math Struct Comp Sci.* 2014;24:e240311.
7. Lutz NW, Schultz E. Phantom material for quantitative evaluation of MR images. *Med Prog Technol.* 1986;11(4):177-84.
8. Raue M, Bernet A, Kuppers M, Stapf S, Schmidt HW, Blumich B, et al. Sodium NMR relaxation: a versatile non-invasive tool for the monitoring of phase transitions and the estimation of effective pore sizes of supramolecular hydrogels. *Intelligent hydrogels. Progress in colloid and polymer science.* Heidelberg: Springer; 2013. p. 45-51.
9. Kopecek J. Hydrogel biomaterials: a smart future? *Biomaterials.* 2007;28(34):5185-92.
10. Mehta M, Madl CM, Lee S, Duda GN, Mooney DJ. The collagen I mimetic peptide DGEA enhances an osteogenic phenotype in mesenchymal stem cells when presented from cell-encapsulating hydrogels. *J Biomed Mater Res A.* 2015;103(11):3516-25.
11. Chaudhuri O, Gu L, Klumpers D, Darnell M, Bencherif SA, Weaver JC, et al. Hydrogels with tunable stress relaxation regulate stem cell fate and activity. *Nat Mater.* 2016;15:326-34.
12. Jensen PA, Bard JF. *Operations Research Models and Methods* Hoboken, NJ, USA: Wiley; 2003.
13. He K, Meeden G. Selecting the number of bins in a histogram: A decision theoretic approach. *J Stat Plan Inference.* 1997;61:49-59.
14. Hargas L, Koniar D, Stofan S. Sophisticated biomedical tissue measurement using image analysis and virtual instrumentation. In: Folea S, editor. *Practical applications and solutions using Labview™ software.* Rijeka: InTech; 2011.
15. Kohler U, Kreuter F. *Data analysis using stata.* College Station: Stata Press; 2005.
16. Frigg R, Werndl C. *Entropy: A Guide for the Perplexed.* In: Beisbart C, Hartmann S, editors. *Probabilities in physics.* Oxford: Oxford University Press; 2011.
17. Güçlü B. Maximizing the entropy of histogram bar heights to explore neural activity: a simulation study on auditory and tactile fibers. *Acta Neurobiol Exp.* 2005;65:399-407.

18. Lutz NW, Viola A, Malikova I, Confort-Gouny S, Audoin, B, Ranjeva JP, et al. Inflammatory multiple-sclerosis plaques generate characteristic metabolic profiles in cerebrospinal fluid. PLOS ONE 2007;2:e595.
19. Marshall I, Higinbotham J, Bruce S, Freise A. Use of Voigt lineshape for quantification of in vivo ¹H spectra. Magn Reson Med. 1997;37(5):651-7.
20. Soher BJ, Wyatt C, Reeder SB, MacFall JR. Noninvasive temperature mapping with MRI using chemical shift water-fat separation. Magn Reson Med. 2010;63(5):1238-46.

Supporting Information

S1 Supplemental Materials 1. Further Methods, Results; Figures S-1 through S-29.

(PDF)

S2 Supplemental Materials 2. Additional Figures S-30 through S-45, Tables S-1 through S-5.

(PDF)

S1 List. Supplemental Lists. Delay lists used in dynamic NMR spectroscopy experiments.

(XLSX)

S1 Video. Horizontal rotation of 3D temperature profiles. Representation based on dynamic NMR spectroscopy experiments.

(AVI)

S2 Video. Vertical rotation of 3D temperature profiles. Representation based on dynamic NMR spectroscopy experiments.

(AVI)